GeoHazards

MDPI

Article

Leveraging Sentinel-2 and Geographical Information Systems in Mapping Flooded Regions around the Sesia River, Piedmont, Italy

George P. Petropoulos [1,*], Athina Georgiadi [1] and Kleomenis Kalogeropoulos [2]

[1] Department of Geography, Harokopio University of Athens, El. Venizelou St., 70, Kallithea, 17671 Athens, Greece; georgiadi.athina@gmail.com
[2] Department of Surveying and Geoinformatics Engineering, University of West Attica, Ag. Spyridonos Str., 12243 Egaleo, Greece; kkalogeropoulos@uniwa.gr
* Correspondence: gpetropoulos@hua.gr

Abstract: Sentinel-2 data are crucial in mapping flooded areas as they provide high spatial and spectral resolution but under cloud-free weather conditions. In the present study, we aimed to devise a method for mapping a flooded area using multispectral Sentinel-2 data from optical sensors and Geographical Information Systems (GISs). As a case study, we selected a site located in Northern Italy that was heavily affected by flooding events on 3 October 2020, when the Sesia River in the Piedmont region was hit by severe weather disturbance, heavy rainfall, and strong winds. The method developed for mapping the flooded area was a thresholding technique through spectral water indices. More specifically, the Normalized Difference Water Index (NDWI) and the Modified Normalized Difference Water Index (MNDWI) were chosen as they are among the most widely used methods with applications across various environments, including urban, agricultural, and natural landscapes. The corresponding flooded area product from the Copernicus Emergency Management Service (EMS) was used to evaluate the flooded area predicted by our method. The results showed that both indices captured the flooded area with a satisfactory level of detail. The NDWI demonstrated a slightly higher accuracy, where it also appeared to be more sensitive to the separation of water from soil and areas with vegetation cover. The study findings may be useful in disaster management linked to flooded-area mapping and area rehabilitation mapping following a flood event, and they can also valuably assist decision and policy making towards a more sustainable environment.

Keywords: remote sensing; GIS; flood; mapping; Sentinel-2

check for updates

Citation: Petropoulos, G.P.; Georgiadi, A.; Kalogeropoulos, K. Leveraging Sentinel-2 and Geographical Information Systems in Mapping Flooded Regions around the Sesia River, Piedmont, Italy. *GeoHazards* **2024**, *5*, 485–503. https://doi.org/10.3390/geohazards5020025

Academic Editor: Tiago Miguel Ferreira

Received: 15 March 2024
Revised: 18 May 2024
Accepted: 20 May 2024
Published: 28 May 2024

Copyright: © 2024 by the authors. Licensee MDPI, Basel, Switzerland. This article is an open access article distributed under the terms and conditions of the Creative Commons Attribution (CC BY) license (https://creativecommons.org/licenses/by/4.0/).

1. Introduction

Climate change can lead to unexpected variation in atmospheric temperature, causing extreme weather conditions (from very high to very low temperatures). Some of the impacts of climate change include increased temperatures, sea level rise, and intense severe weather events like droughts and floods [1,2]. Floods are one of the most frequent, destructive, costly, and widespread natural disasters worldwide [3–6]. Floods are known to affect societies, economies, and ecosystems and, at certain times and places, can have devastating impacts [7,8]. They cause casualties and property damage [3] on every inhabited continent and cause severe losses that negatively affect regional socio-economic development, industry, agriculture, and infrastructure [5], as well as cultural heritage [9–11]. The reason for flood generation is mainly due to heavy or prolonged rainfall and can have significant impacts on the water load of rivers, streams, and canals. Wang et al. [12] projected that the losses and risks linked to floods are higher than those of any other climate risk.

The phenomenon of climate change and the presence of more and more frequent extreme weather events are intensifying the generation of larger and more destructive flood events. Commercial and residential area expansion has led to the development of societies

in coastal areas and river basins, which are among the areas prone to flood risks. In addition to the more pronounced presence of climate change, increased instances of flooding are linked to population growth [13,14]. In light of global warming, these losses will continue to increase in the future, as the intensity of extreme rainfall increases and, at the same time, the population exposed to water-related disasters increases. Hence, flooding around the world, which is continuously increasing, makes it necessary to manage it to urgently address the increasing flood risk [12]. Looking at flooding spatially, developing countries are affected more and for a longer period of time by natural disasters [15]. This is happening due to the combination of adverse climatic conditions and unstable geo-analysis with deforestation, the haphazard expansion of spatial development, haphazard construction making them prone to disasters, areas being more vulnerable, poor or non-existent funding for prevention, and delayed or non-existent communication with vulnerable populations [16].

Nevertheless, both developing and developed countries continuously face the risk of flooding. Predictive analyses of future flood risks divulge that the growing influence of climate change, coupled with inadequate preparedness against such flood events in many regions around the world, will end in a historically high level of flood-related losses. In Italy, flooding remains a serious risk, particularly in the north in the valleys through which the rivers Padova and Arno flow. The heavy rainfall in Northern Italy makes many areas particularly vulnerable to flash flooding [17]. For this reason, it is of paramount importance to find effective ways of managing disaster risk [18] where it is deemed necessary that a high risk of flooding is observed, for example in Northern Italy.

In a general context, flood management includes the forecasting, detection, mapping, evacuation, and relief activities of a flood. It is important to focus on ways to mitigate floods and provide a rapid response afterwards to minimize fatalities and reduce environmental and economic damage. The accurate mapping and modelling of floods are essential in flood risk assessment, damage assessment, and sustainable urban planning for proper flood risk management [19]. Crisis response agencies are turning to satellite flood mapping to obtain a comprehensive picture of flooded areas [20,21]. As such, satellite remote sensing (RS) is currently a low-cost tool that can be used in mapping flooded areas [19,22,23].

Satellite remote sensing and Geographic Information Systems (GISs) are powerful tools that offer significant advantages, particularly in disaster management [24–27]. Some of these include the ease of providing summary information for large areas at low cost, data reliability, overcoming spatial barriers such as accessibility to the location of interest or locations with hazardous environmental conditions, etc. [9,28,29]. Moreover, satellite remote sensing provides a concise and continuous real-time coverage of the flood event being studied [20]. Therefore, it seems reasonable that in situations where there are flooded areas and due to the poor accessibility to these areas and the prevailing weather conditions, the use of satellite data is a very appropriate solution to capture this natural disaster.

In remote sensing images, flooding is characterized by clear boundaries. Therefore, many recent studies have extracted flood coverage from satellite data [22,30–32]. The remote sensing data most commonly used to map a flooded area are spectral data from optical sensors or backscatter data from synthetic aperture radar (SAR) [33]. Spectral data from optical sensors are highly correlated with open water surfaces [34]. This is also the preferred data source for flood mapping, but under cloud-free conditions, as they provide high spatial and spectral resolution [31]. However, one of the severe limitations stemming from optical imagery is its inability to penetrate the cloud cover that frequently exists during large-scale flooding caused by rainfall [35,36].

SAR (which records energy reflectance-based data) can detect water independently of interference that clouds can create and is also effective during day and night [37]. However, limitations such as the inability to differentiate between water and water-like surfaces, speckle-like spots, and geometric correction properly, may hinder global flood mapping applications using radar data [12,36–38]. In contrast to spectral data, SAR data are particularly attractive for disaster monitoring due to the ability to collect day/night and all-weather images [4,39]. However, optical satellite images contain rich information in their

bands [40], which has a preferable effect on land cover classification [4,34,41]. In general, SAR and multispectral techniques are capable of accurately extracting water features if there is substantial contrast between water and non-water features in the data [42].

GISs are capable of producing a flood risk map by delineating areas prone to flooding. With this map, the potential impacts of a flood disaster can be quickly assessed and appropriate control measures can be taken to mitigate the predicted catastrophic effects of flooding. In addition, they provide a wide range of tools for identifying areas affected by flooding or predicting areas likely to be inundated by significant flooding. They also facilitate the geographic storage of information in a database that can be searched and analyzed graphically [43]. GISs in flood management are employed not only to visualize the extent of flooding but also to further analyze this product to quantify the potential damage caused [43,44].

In view of the above, this study aimed to develop a threshold-based image processing technique for mapping flooded areas from Sentinel-2 multispectral satellite data and GIS analysis. In this framework, two such techniques were used and compared against each other, exploiting as a reference the flooded area derived from the Copernicus Emergency Mapping Service (EMS), which provides ready-made products for mapping natural disasters such as flooded areas. Therefore, the main research questions of this work were as follows: how do the Normalized Difference Water Index (NDWI) and the Modified Normalized Difference Water Index (MNDWI) indices compare in accurately mapping flooded areas, and what insights can be gained for improving flood mapping techniques using Sentinel-2 satellite data? These indices have been used in several studies, such as flood monitoring, waterlogging, flood mapping, flood inundation, water detection, etc. [45–50]. As a case study, the flooding event of the Piedmont region of Italy that occurred on 3 October 2020 was chosen.

2. Materials and Methods

2.1. Study Area

The Sesia River (Figure 1) is located in the Sesia-Val Grande geopark and is one of the longest rivers in the Piedmont (Piemonte) region, as it also has short tributaries in Lombardy (138 km) and is an important tributary of the Po [51–54]. It emerges from Monte Rosa at an altitude of about 2500 m from the homonymous glacier. It then flows very rapidly downstream to Valsesia, receiving in this section the waters of numerous streams, which greatly enrich its flow [51,55]. According to the Po River Basin Authority (Autorita di Bacino del fiume Po Parma), the Sesia River Basin has a total surface area of about 3075 km^2 (4% of the surface area of the Po River Basin), 45% of which falls in mountainous areas. Sesia and its tributaries Mastallone, Sessera, and Cervo, with the Elvo tributary, come from the same orographic complex. Their respective basins are responsible for high annual precipitation values, as well as short and intensive rainfall, which give rise to a flow regime characterized by a high frequency of flooding events with significant flow rates in the peak period [56,57].

Sesia River, although benefiting from the nival supply of the Monte Rosa glacier, is a highly torrential river: with an average high flow rate of 76 m^3/s, it can suffer very low flows in the driest summers (even very few mc/s), mainly due to the very intensive exploitation of its waters for irrigation and flooding of rice fields. On the contrary, in cases of exceptional rainfall in Upper Valsesia (such as in 1968, 1994, or 2000), the river can even reach impressive flood rates of 5500–6000 mc/s, the highest ever recorded among the tributaries of the Po, to the point where it significantly affects flooding. Then, from the confluence with the Celvo, the regime becomes much more normal. The altitude of the area ranges from 190 m altitude in the lower alpine area of the Piedmont region to 4554 m altitude at the top of Monte Rosa (Pennine Alps), the second highest mountain range in Europe's Alps. Indeed, the area is predominantly mountainous, including high and large flood plains, as well as a part of Lake Maggiore [58].

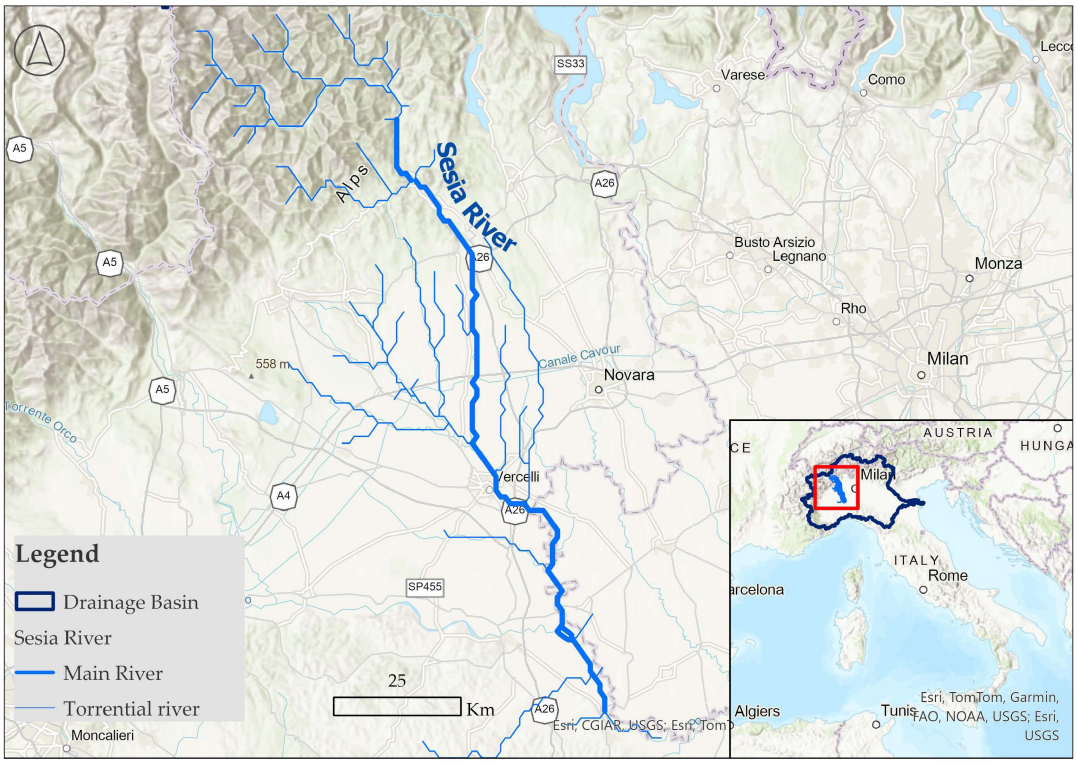


Figure 1. Location of the study area. Sesia River, Piedmont, Italy.

As for the event, from the early hours of 3 October 2020, severe weather disturbance hit Northern Italy, with heavy rainfall and strong winds. The highest damage was reported in the Liguria region and in the northern and western part of the Piedmont region, where recorded rainfall exceeded the previous historic level of 1958 (the total rainfall amount in 1958 was 196.8 mm) [59,60]. Also, there are many floods recorded in this area [61]. For example, on 15 September 2006, a rainfall of 181 mm occurred [62]. The mean annual rainfall in the whole catchment is 1013 mm, while the mean annual discharge is about 70 m^3/s [63].

The heavy rainfall (450 mm [54]) caused many rivers to overflow and caused flooding in many areas. The Sesia River overflow in the Piedmont region caused road closures, the collapse of the bridge, and flooding in several areas. In addition to material damage, however, two human casualties were recorded. The Sesia River rose rapidly, destroying the valley floor. Estimations of the maximum discharge sit at about 3000–5000 m^3/s [54].

Flooding with infrastructure damage occurred throughout Valsesia. Significant damage to crops and houses also occurred in the lower Vercelli area: Borgo Vercelli was partially flooded, as was the Turin–Milan railway line between Bivio Sesia and the SP12 railway bridge at Borgo Vercelli [61,64,65].

2.2. Datasets

In this study, the multispectral data of the Sentinel-2 satellite were selected as the main data. This choice was made as multispectral imagery has been successfully used to monitor water bodies and rivers, detect changes, and extract water characteristics [22,40,48,49,66–70]. Furthermore, when cloud cover is not a major issue, the application of optical remote sensing to floodplain maps offers the possibility of reliably but also quickly identifying hazardous areas and supporting the implementation of response activities and flood coping strategies.

The Sentinel-2A and 2B satellites carry an innovative high-resolution multispectral camera with 13 spectral channels to record terrain and vegetation with high accuracy (Table 1). The Sentinel-2 satellite, in addition to its important capability by design for

emergency management, includes multispectral imaging instruments for environmental monitoring and management in general and in particular for the study of water and hydrographic networks, land cover, and vegetation in coastal areas. In addition, it is considered suitable for the recording and continuous imaging of natural disasters such as floods. Sentinel-2 data are the highest spatial resolution multispectral remote sensing data currently available to the public free of charge on the European Space Agency (ESA) Copernicus Open Access Hub website (https://scihub.copernicus.eu/, accessed on 2 May 2024). Sentinel 2A was launched in June 2015 and Sentinel 2B in March 2017. It has different spatial resolutions and varies from visible and near-infrared to short-wavelength infrared (Table 1). The Sentinel-2 multispectral level 2A (L2A) level data contain atmospheric bottom reflection products corrected for the atmosphere [5]. For the selected case study, the images had a spatial resolution of 10 or 20 m and were taken before the flood on 28 September 2020 at 10:20:31 and after the flood on 3 October 2020 at 10:17:59.

Table 1. Details of the used Sentinel 2A and 2B data.

Spectral Band	Band	Wavelength (µm)	Spatial Resolution (m)
Blue (B)	B2	0.46–0.52	10
Green (G)	B3	0.54–0.58	10
Red (R)	B4	0.65–0.68	10
Red edge (RE1)	B5	0.698–0.712	20
Red edge (RE2)	B6	0.733–0.747	20
Red edge (RE3)	B7	0.773–0.793	20
Near-infrared (NIR)	B8	0.784–0.9	10
Near-infrared (NIR)	B8A	0.855–0.875	20
Shortwave infrared (SWIR1)	B11	1.565–1.655	20
Shortwave Infrared (SWIR2)	B12	2.1–2.28	20
Date/hour (pre-flood)		28 September 2020, 10:20:31	
Date/hour (post-flood)		3 October 2020, 10:17:59	

The images are L2A, have undergone geometric, radiometric, and sensory correction, are correct for the format as well as the overall quality, and have reflectivity values.

Additional data were considered such as the polygons of Europe and the polygon of Italy (vector data). They are the backgrounds for the completion of some treatments and the creation of some maps. These were retrieved from Efrain Maps, an open geospatial data website (https://www.efrainmaps.es/english-version/free-downloads/europe/ accessed on 2 May 2024) and the European Environment Agency (https://www.eea.europa.eu/data-and-maps/data/eea-reference-grids-2/gis-files/italy-shapefile accessed on 2 May 2024), respectively. Finally, the points of the most important Italian cities and the hydrographic network, also in vector format, were retrieved from the MapCruzin.com website (https://mapcruzin.com/free-italy-arcgis-maps-shapefiles.htm accessed on 2 May 2024).

For validation purposes, data from the EMS were also used. The validation data used in the present study consist of the mapped flooded areas from EMS for the event that occurred on 3 October 2020 for the Sesia River. The first product estimate was obtained from the Sentinel-2 satellite image from 3 October 2020 at 10:27 UTC. The result of the event service consists of 6 map products.

2.3. The Methodology

To achieve the objectives of this work, Sentinel-2 satellite data were chosen to be used, where they were processed in the Sentinel Application Platform (SNAP) software version 9.0 (https://step.esa.int/main/download/snap-download/ accessed on 2 May 2024), and then the final maps of the flooded areas of the two techniques were extracted using QGIS software (https://www.qgis.org/en/site/ accessed on 2 May 2024) (Figure 2). The basic pre-processing of the data was carried out, and then the application of the indicators and the detection of flooding changes to the satellite images was carried out. The last step was the validation of the mapping techniques using the data from the EMS. Data processing was

conducted using SNAP software, with the final maps exported to QGIS for visualization and analysis. The steps of the methodology are summarized in Figure 2.

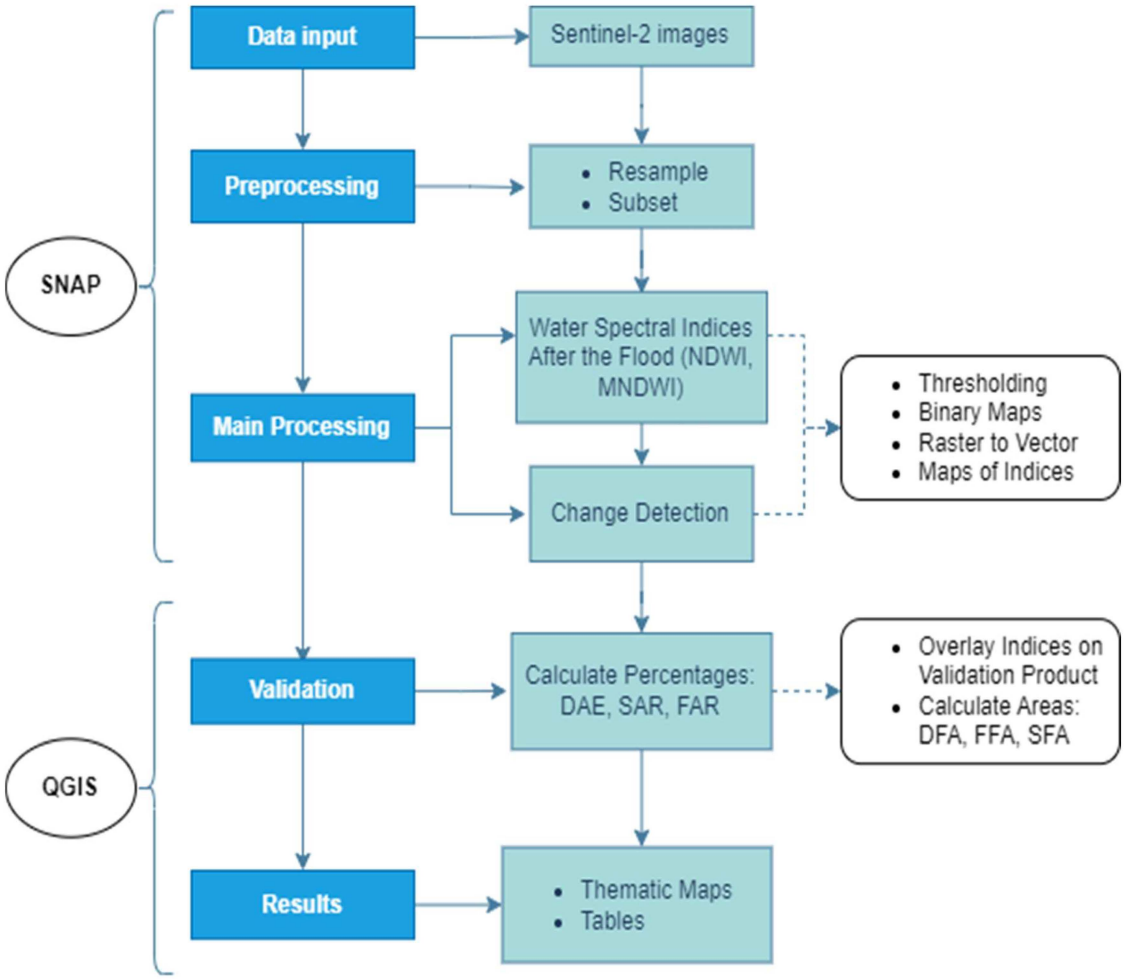


Figure 2. Flow chart of the flooded-area mapping methodology.

2.3.1. Data Pre-Processing

Initially, the SNAP software was used to pre-process the Sentinel-2 images before applying the two mapping techniques. The main steps of the pre-processing before and after flooding are summarized as follows:

The Sentinel-2 images contain 13 spectral channels at three different spatial resolutions (Table 1). Therefore, we chose to resample the images at 20 m. In short, this procedure converts the spatial resolution of all channels to the same measures and was applied to both images in the methodology.

The broader post-flood image showed several clouds in the northern part of the image but very few over the flooded area. Therefore, the images were cropped to a smaller area of the flooded study area. This facilitated both image processing and the absence of errors due to cloud cover. The location where the techniques were chosen to be presented is representative and is the central extent of the floodplain, as it is still adjacent to a habitable area. This operation was applied to both images of the methodology.

Figure 3 shows the pseudo-color images of the cropped area before and after the flood. It can be observed that shades of red indicate areas where vegetation (RGB: B8, B4, B3) is present, and more specifically, where the shades are more intense means that they show forested area, while areas where they are lighter represent cultivated areas. The post-flood image shows more intense shades of red, as the vegetation has just been affected by the rain and therefore has a higher concentration of water. By comparing the images before

and after the flood, it is evident that the river's boundaries before the flood were much more restricted and were close to residential areas.

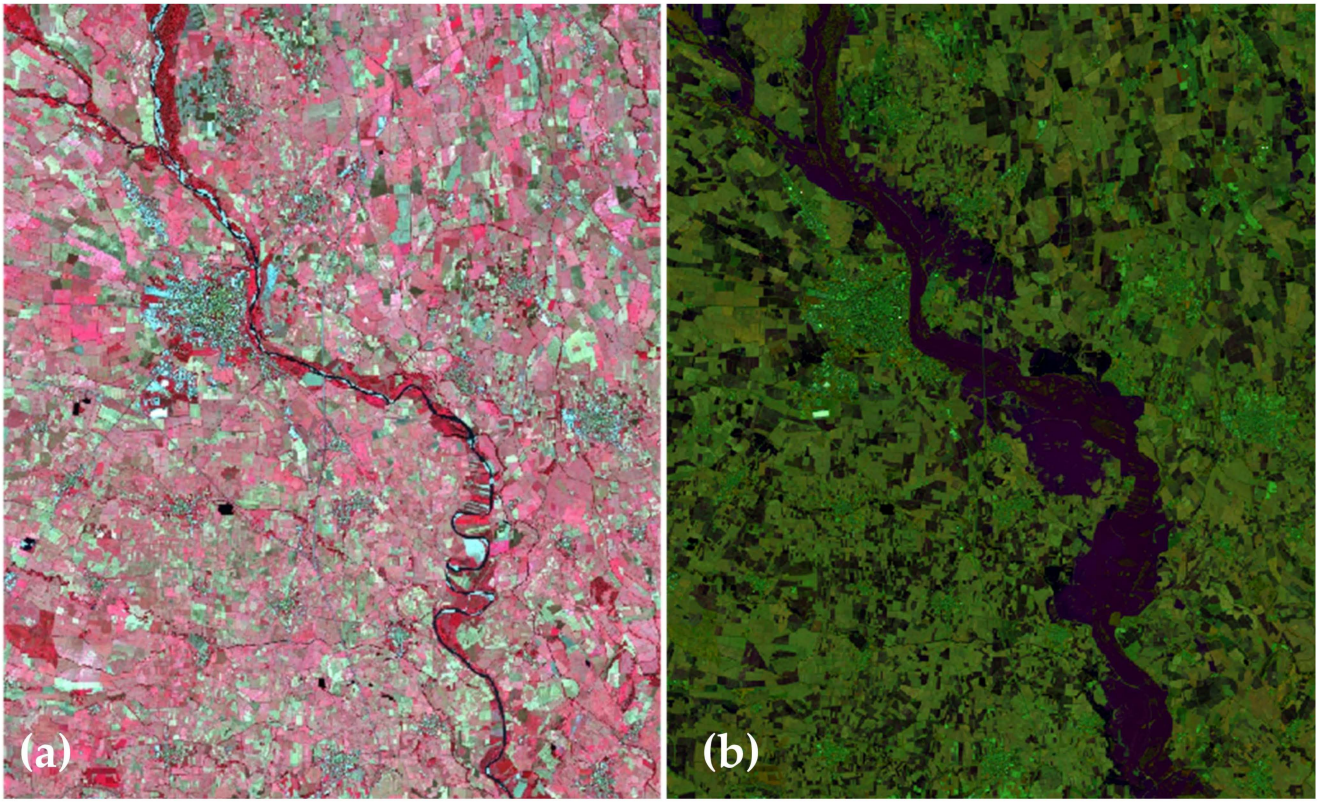


Figure 3. (**a**) Pseudo-color comparison of study area pre-flood (28 September 2020, 10:20:31) and (**b**) post-flood (3 October 2020, 10:17:59).

As part of the initial pre-processing, we opted to crop the Copernicus validity product to match the extent of the cropped Sentinel-2 images in the same area (Figure 4).

2.3.2. Main Processing

The main processing of the data involved flood mapping and change detection. For this purpose, thresholding was applied using spectral water indices such as the Normalized Difference Water Index (NDWI) and the Modified Normalized Difference Water Index (MNDWI) to pre- and post-flood images. A sub-stage of the main processing is a change detection approach. This technique was applied to the image just after the flood; i.e., a monochronic approach was followed.

The indices applied were the NDWI (Equation (1)) and the MNDWI (Equation (2)). The NDWI was originally proposed by McFeeters [71] and is designed to maximize the reflectance of water bodies in the green band and minimize their reflectance in the near-infrared (NIR) band. The MNDWI can effectively suppress and even remove the noise of building construction as the NIR band is replaced with the short-wave infrared (SWIR) band [39]. The equations of the indices are as follows:

$$NDWI_{McFeeters} = \frac{\rho_{Green} - \rho_{NIR}}{\rho_{Green} + \rho_{NIR}} \quad (1)$$

$$MNDWI = \frac{\rho_{Green} - \rho_{SWIR}}{\rho_{Green} + \rho_{SWIR}} \quad (2)$$

After the application of the indicators, a threshold had to be applied in order to distinguish the flooded area more easily. The thresholds were selected after observing the histograms of the indicators. Observing the histogram for the post-flood image of the

NDWI (Figure 5), it was verified that it shows two peaks, which means that the pixels' values at these points are more concentrated. Looking also at the values of the pseudo-color index image (Figure 6a), one can be observe which pixels represent the flooded area, where they are distinguished by shades of orange. The value that best separates the two peaks was chosen as the threshold in this case, where the point is −0.026 (Figure 6b).

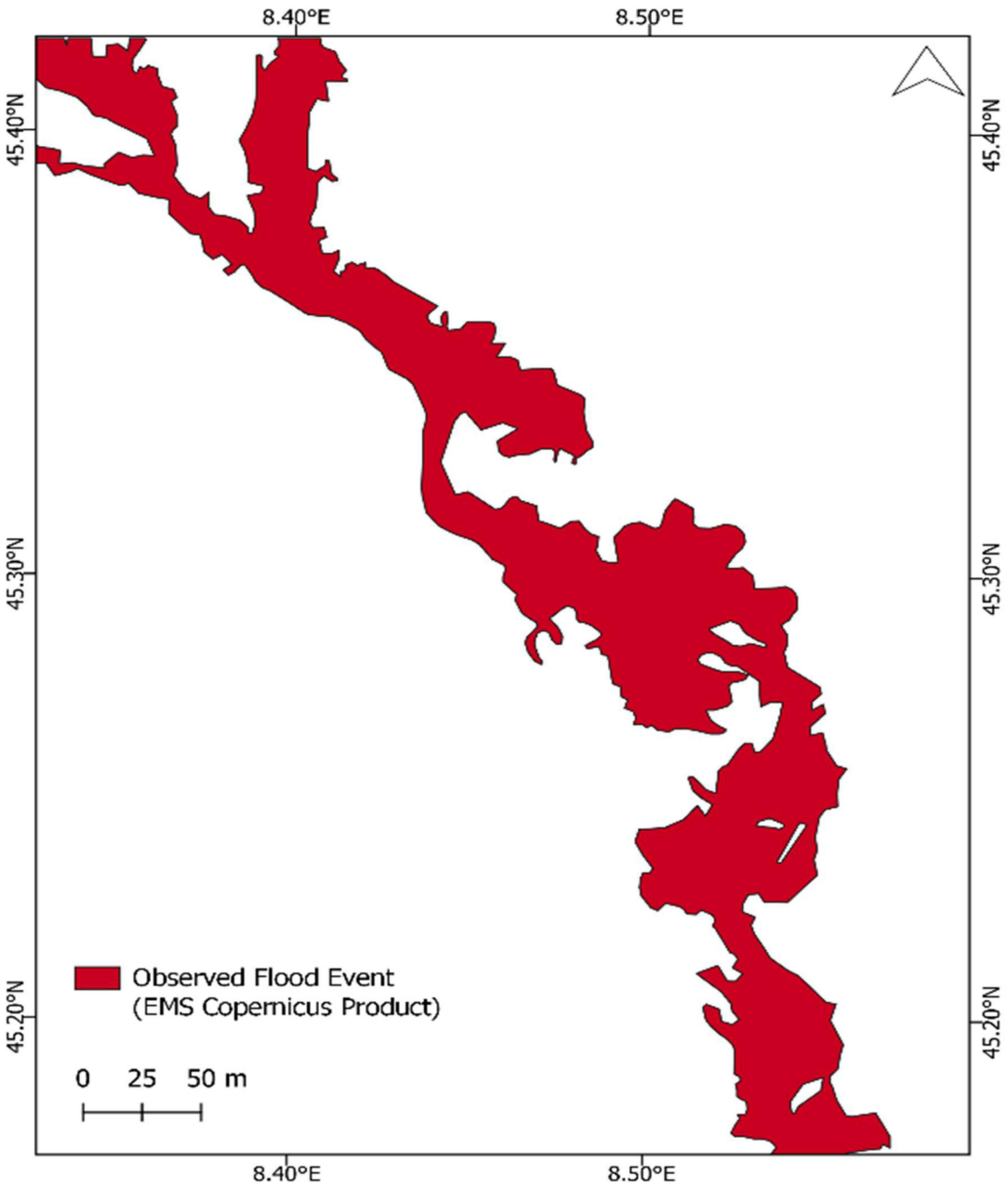


Figure 4. Polygon representation of processed flooded areas in the EMS assessment product.

The same threshold selection procedure was applied for the MNDWI before the flood. In the histogram of this index (Figure 6c), two peaks are again observed, where the intermediate point that discretely separates them is −0.43 (Figure 6b). Looking even at the table of pixel shades, it can be seen that the dark-red pixels of the index are also the ones that capture the flood.

Opting to round the pre-flood indicators to the third decimal place (Table 2) was intended to maximize the coverage of the water bodies.

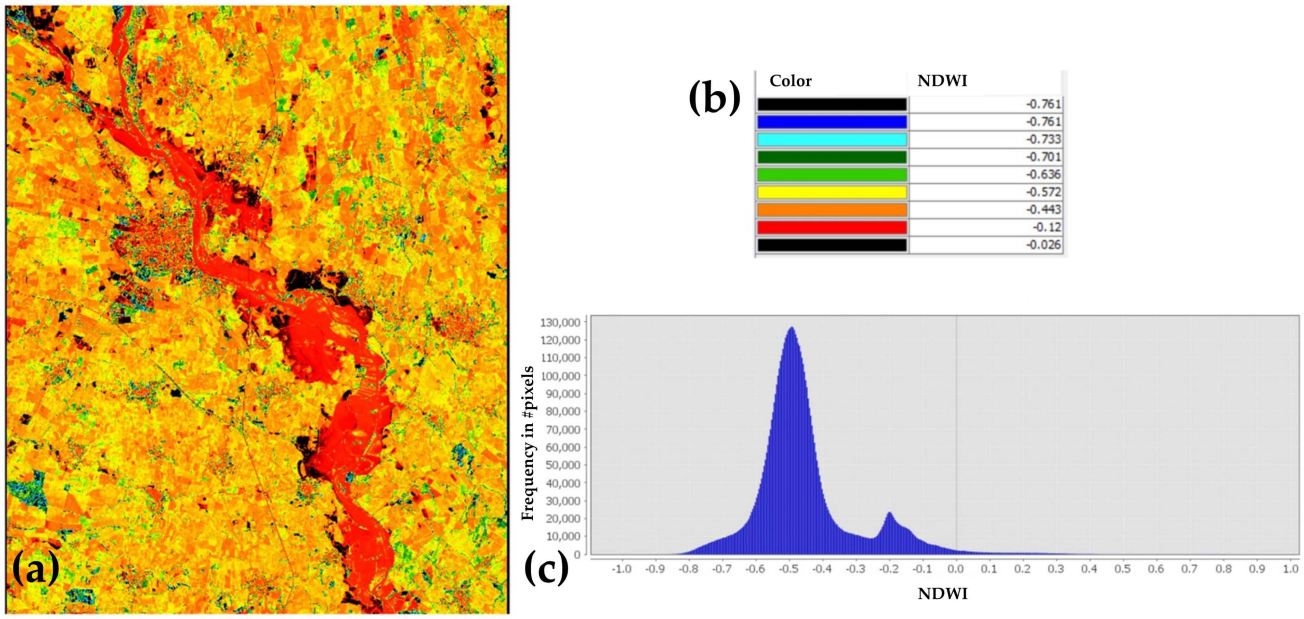


Figure 5. (**a**) Pseudo-color representation of NDWI post-flood, (**b**) pixel value visualization, and (**c**) histogram analysis.

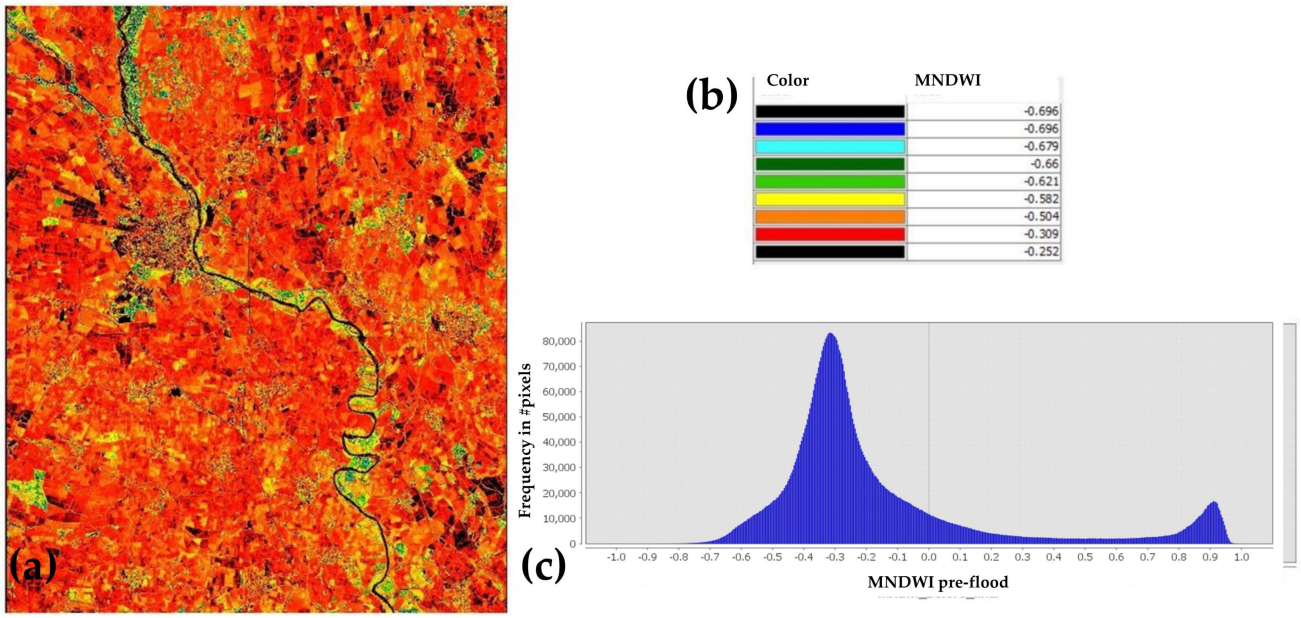


Figure 6. (**a**) Pseudo-color image of the MNDWI pre-flood, (**b**) pixel value visualization, and (**c**) histogram analysis.

Table 2. Threshold limits applied to indicators before the flood.

	Threshold	
	NDWI	**MNDWI**
Pre-flood	if NDWI ≤ -0.252, then 1; otherwise, 0	if MNDWI ≤ -0.253, then 1; otherwise, 0

After the thresholds were applied, two binary images were created, showing the flooded areas as 1 and all other information in the image as 0. Subsequently, the pre-flood index data underwent importation into QGIS. To ensure compatibility, all data utilized were standardized to the same format, necessitating the conversion of raster images to

vector format (in WGS 84). At this stage, it was necessary to overlay the index layers with the EMS result validity product in order to remove all non-flood data in the index images that are shown as flooded, even if they are not.

Change detection is the process of identifying differences in the state of an object or phenomenon by observing it at different times [41]. By change, we mean changes in surface components at different rates. The principle of change detection in remote sensing determines that changing land cover will change the spectral properties of an area. It is also preferable to utilize the same sensor with proximate acquisition dates, which can be challenging, particularly when considering cloud cover. In this case, this problem was not addressed because the dates of the two images are not distant and the cropped images do not show clouds. One method used was map algebra, which by threshold selection identifies the altered regions through the calculation of a spectral index. Its advantages are that it is relatively simple, easy to interpret, and can handle lighting phenomena, and yet, it does not fully exploit the spatial context of real-world objects. Although, the success of the technique depends on selecting the appropriate band or indices and choosing the appropriate thresholds [72].

This technique was applied to two different images, one a few days before the flood and one just after the flood. Thus, a multi-temporal approach of mapping the flooded area was used. The mapping methodology for the image just after the flood was discussed in detail previously.

The steps followed to implement change detection are to subtract the area of each indicator before the flood from the area of each indicator after the flood. The result of this process produces a map for each indicator showing the flooded area, excluding the original river area. Finally, a threshold was applied to the difference image to accurately identify areas that have undergone a change in water content.

2.3.3. Validation

The accuracy of flooded-area detection, which has also been used effectively in other studies [40], was next evaluated. The accuracy of flooded-area estimates was expressed in terms of detected area efficiency (DAE, Equation (3)), skipped flooded-area rate (SFA, skipped area error, Equation (4)), and false flooded-area rate (FFA, assignment error, Equation (5)) [44]; the aforementioned equations are presented below:

$$Detected\ Area\ Efficiency = \frac{DFA}{DFA + SFA} \quad (3)$$

$$\text{Skipped Area Rate} = \frac{\text{SFA}}{\text{DFA} + \text{SFA}} \quad (4)$$

$$False\ Area\ Rate = \frac{FFA}{DFA + FFA} \quad (5)$$

where

DFA is the detected flooded area, i.e., the common area between the polygon of the generated flooded area and the polygon of the validity product.

FFA is the false flooded area, i.e., the area included in the polygon of the generated flooded area but not in the polygon of the validity product.

SFA is the skipped flooded area, i.e., the area included in the polygon of the validity product but not in the generated polygon.

All processes at this stage were conducted in QGIS. The validation of the results was performed using the Copernicus validity product, where initially, the areas of the indices before the flood were removed for each index separately. For the NDWI, the flooded-area result had to be merged with the validity product. Then, the intersection of the merged polygon created with the validity product had to be performed to create the DFA, the common area, and the SFA, the area present in the product but not in the index. Next,

the difference function of the index result with the product was applied to create the FFA, which represents the falsely flooded area present in the index but not in the product.

The only difference in the process followed for the MNDWI was that instead of applying the intersection of the merged polygon, the clip function of the merged polygon from the validity product was applied. Then, the DFA and SFA areas were created. Additionally, the road network line falsely represented as flooded area was removed from the difference result of the index. Thus, the final thematic maps of the validity control of the results were extracted, depicting the DFA, SFA, and FFA areas. Finally, the areas mentioned were calculated, the equations of Detection Accuracy Error (DAE), Sensitivity (SAR), and False Alarm Rate (FAR) were applied, and the final thematic maps of the validity control of the results were created.

3. Results

The results of the applied techniques are presented, namely the main processing involving the application of NDWI and MNDWI indices after the completion of the analysis on Sentinel-2 2A images before and after the flood.

The maps in Figure 7 present the processed polygons of the results of the flooded area based on the NDWI and MNDWI indices, respectively. Making some comparisons between the two maps, it is observed that the results seem to have no significant differences. The NDWI shows a vertical area almost at the central point of the flood, which was incorrectly classified as flooded, while in reality, it is part of the area's road network. The MNDWI, on the other hand, was observed not to encounter problems with distinguishing and categorizing linear entities and thus completely removed the road network from its depiction as a water surface. Additionally, the NDWI during its application also characterized most of the residential area at the northwest point of the image as a water region, a fact that was not observed in the MNDWI. This was observed in the comparison of the produced indices and the satellite image after the flood.

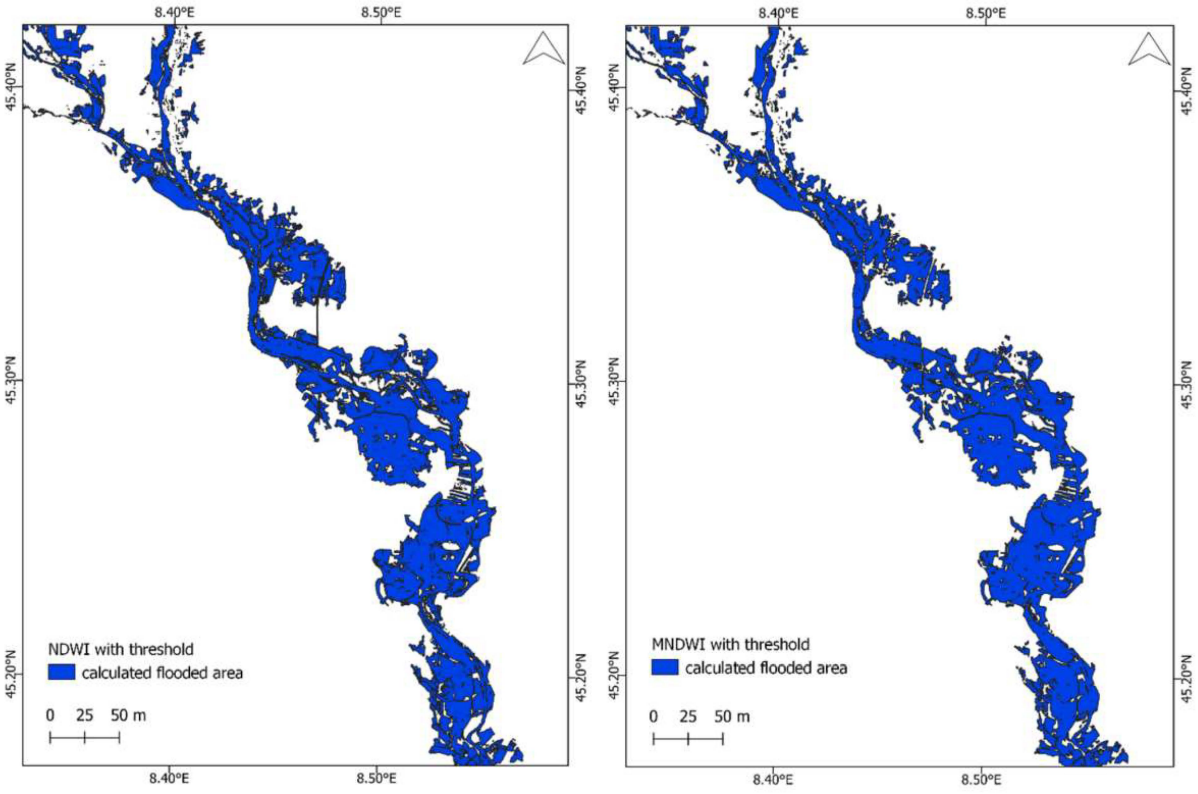


Figure 7. The final results of the flooded areas based on the NDWI (**left**) and MNDWI (**right**) indices after the flood.

Finally, the extent of the flooded area for the NDWI was calculated to be 59.51 km^2, while for the MNDWI, it was 58.02 km^2. This means that the estimated flooded area for the first index was slightly overestimated compared to the second index. The difference between the two indices amounts to 1.49 km^2.

The maps in Figure 8 show the results of the river area indices before the flood. The final step of the main processing, involving change detection, was the subtraction of the pre-flood index result from the post-flood index result. Observing the results of the indices before the flood, they do not seem to exhibit significant differences between them. The boundaries of the river appear to be quite distinct in both the NDWI and MNDWI indices. However, different entities, apart from water, were observed to be more pronounced between the indices. Regarding the NDWI, before the flood, it presented the structured area and the road network more prominently. This could be attributed to the threshold applied or to the fact that the MNDWI detects water better when there is more vegetation and structured area in the image.

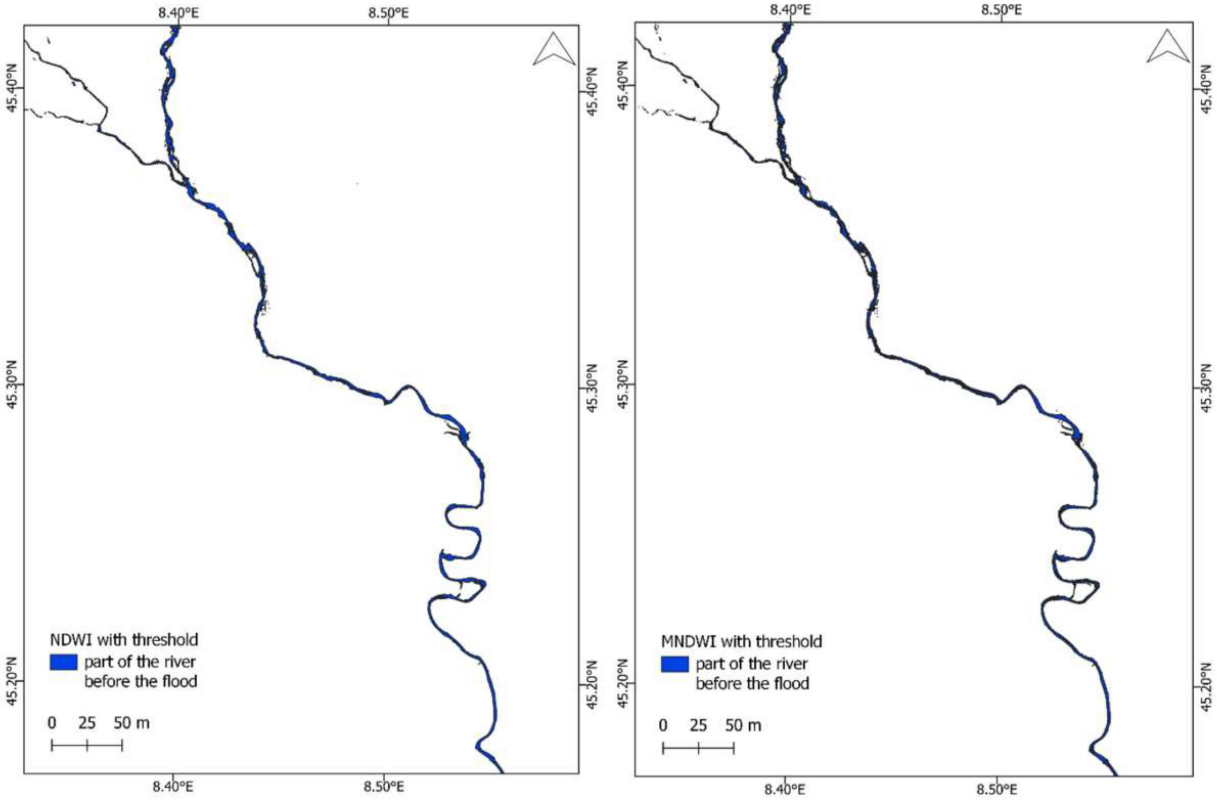


Figure 8. The final results of the flooded areas based on the NDWI (**left**) and MNDWI (**right**) indices' outcomes pre-flood.

Having applied change detection to the indices calculated before and after the flood, the results of the final products were calculated by subtracting the initial river surface. The validity of the results was also verified in these steps (Figure 9).

Regarding the extent of the flooded area, it was calculated to be 54.50 km^2 for the NDWI and 53.23 km^2 for the MNDWI. This means that the calculated flooded area for the NDWI was slightly overestimated compared to the MNDWI. The difference between the two indices amounts to 1.27 km^2. In this technique, it was observed that the calculated area by the NDWI was again slightly overestimated compared to MNDWI, but their difference is slightly smaller.

The validity check results consist of two final maps (Figure 10) for the NDWI and MNDWI indices, respectively. In the maps, areas with common flood extents between the computed index and the validity product are symbolized with DFA (green), while areas

appearing only in the validity product are symbolized with SFA (light yellow), and areas calculated only by the indices and not by the product are symbolized with FFA (red).

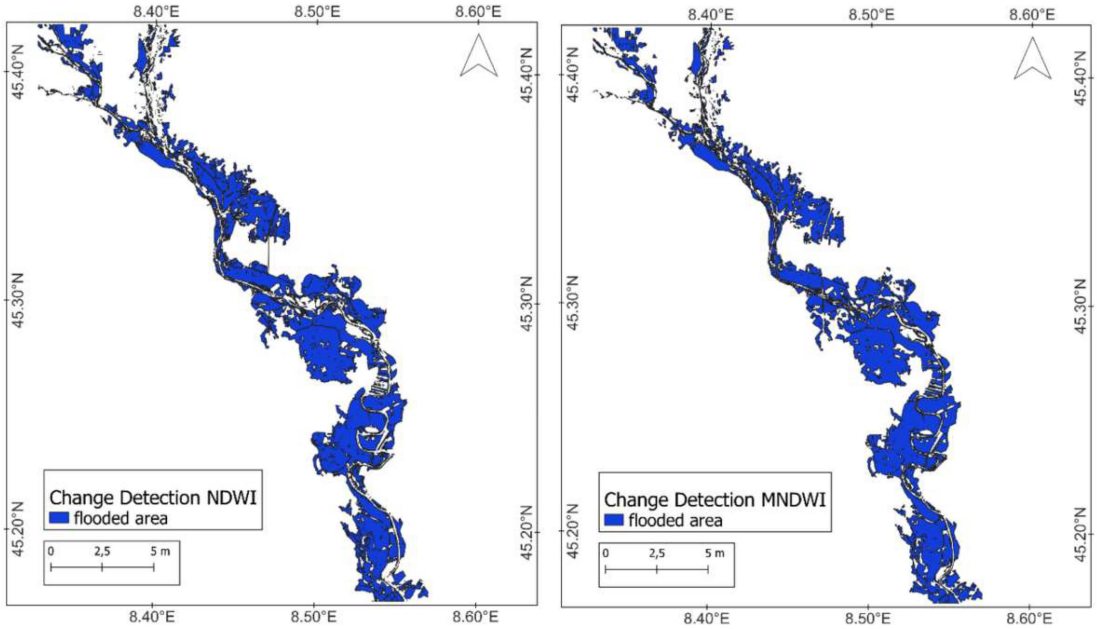


Figure 9. Final comparison of flooded areas based on the NDWI and MNDWI indices; the studied area is depicted.

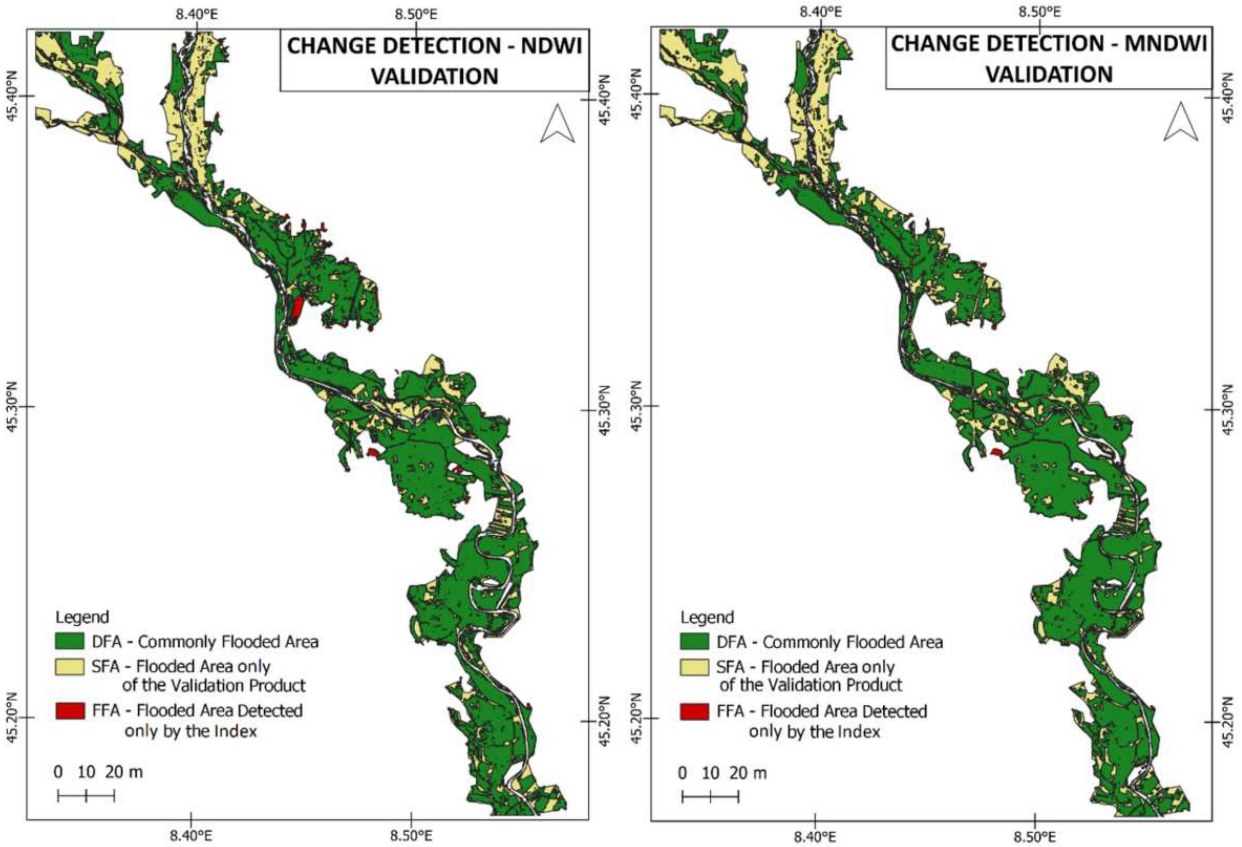


Figure 10. Thematic validation of the flooded areas comparing the NDWI (**left**) and MNDWI (**right**) results.

Combining both techniques, the greater representation of the SFA area is found at the branching of the northwestern part of the flood. This means that the flooded area calculated by the validity product does not coincide with the representation of the flooded area by the computed indices. Finally, the FFA areas between the calculated indices seem not to be common in some points.

As observed in the next table (Table 3), the highest value of the DFA area was distinguished in the NDWI, at 52.91 km^2. However, the difference in DFA between the MNDWI indices was only 0.43 km^2, indicating that the differences in DFA between the two indices were very small. Regarding the FFA areas, the MNDWI presented a higher value, meaning better results in finding fewer areas that were outside the boundaries of the validity check product, with an area of 0.75 km^2. The NDWI presented slightly more than twice the value of FFA areas. Additionally, for the SFA areas, both indices showed similar values, with the MNDWI appearing to have slightly missed the representation of flooded areas compared to the validity check product, omitting an area of 24.76 km^2, with the difference from the NDWI at 0.60 km^2. In summary, the examination of the areas seems to present similar results for DFA and SFA areas, while for FFA areas, the difference between the two indices is almost double. In conclusion, the NDWI presents slightly better results in representing DFA and SFA areas while also including more FFA areas outside the validity product. This can be attributed to the fact that the NDWI in this study area showed slightly better results and has slightly higher accuracy than the MNDWI.

Table 3. Summary of comparisons of inundated areas with validation product of results with NDWI and MNDWI techniques.

Water Spectral Indices with Change Detection						
Change Detection	**DFA (km^2)**	**FFA (km^2)**	**SFA (km^2)**	**Detection Efficiency Rate (%) [DFA/(DFA + SFA)]**	**Commission Error (False Area Rate) (%) [FFA/(DFA + FFA)]**	**Omission Error (Skipped Area Rate) (%) [SFA/(DFA + SFA)]**
NDWI	52.91	1.59	24.15	0.687	0.029	0.313
MNDWI	52.48	0.75	24.76	0.679	0.014	0.321

As for the percentage of detection effectiveness (Detected Area Rate (DAR) %), based on the DFA areas of the indices, they are similar, with the NDWI showing slightly better results of a few decimal points at 0.687% compared to 0.679% for the MNDWI. Additionally, the commission error rate (False Area Rate (FAR), commission error %) seems to be higher for the NDWI (commission error = 0.029%). The omission error rates (Skipped Area Rate (SAR), omission error %) between the two indices were calculated to be quite similar, with the NDWI showing 0.313%, which may be attributed to the justification of the SFA areas.

4. Discussion

For the images before and after the flood, the NDWI presented better classification results for the water pixels. This can be easily attributed to the fact that before and after the flood, the detection of surface water in the area did not include high vegetation. In contrast, the MNDWI can provide accurate results in areas with vegetation, such as cultivated land in this case, which is why the NDWI presents better results for the images. However, the difference between the two indices is minimal. Nonetheless, observing only the results of the final maps, it becomes apparent that, in many points, the indices for the mentioned areas presented different results. This is due to the fact that the indices use different spectral channels in water detection, so the neighboring pixels in water will be influenced differently depending on the entities around them, affecting their reflectance. The MNDWI was observed to be more sensitive in separating structured areas and road networks from flooded ones compared to the NDWI.

Based on the results of the validity check, it becomes evident that the techniques provide greater detail in depicting the flood. The final maps show that the indices better

capture the flood. Specifically, the NDWI seems to have slightly more similarities with the validation product (DER = 0.687%) compared to the MNDWI (DER = 0.679%). Common areas characterized by the Copernicus product are apparent in the branching of the northern and central parts of the flood. Thus, the validity checks revealed moderate mapping results for the flooded areas. These low percentages are also due to the fact that the northeastern point of the river's branching in the pseudo-color image appears to have a forested area, which has been erroneously classified as flooded in the validation product. Therefore, it is understandable that the primary source of errors is due to the selection of the validation product for result validation.

The techniques demonstrated high accuracy levels, observed in delineating flooded areas, making them suitable candidates for incorporation into flood warning tools. The areas that show worse results are those characterized as transitional, meaning they exhibit structured, forested, or cultivated areas. In conjunction with the validation product that classified a larger area as flooded, it is reasonable before the application of the techniques to compare the image used for mapping with the product selected for result validation. With this observation, it can be evaluated whether the validation product is suitable for use and processing.

The selection of the specific techniques for flood mapping was not incorrect, but the choice of the validation product for result validity was. Specific errors encountered included the presence of cloud cover in the Sentinel-2 image before the flood, which was addressed by cropping the image to a smaller extent. An additional error that was removed during validity checking was the straight section of the road network of the NDWI. The use of the appropriate threshold can also introduce errors in pixel classification and is necessary in distinguishing water surfaces as accurately as possible.

The major problem encountered in computational speed during data acquisition was the retrieval of Sentinel-2 images, as well as the application of techniques with the selection of the appropriate threshold for capturing the best spatial resolution of the index.

In other studies where a similar approach was used, the results of the indices showed very good flood mapping results [22,40,73–77]. The NDWI is more accurate than the MNDWI for extracting surface water with vegetation from Landsat data [78]. The NDWI appears to be more sensitive in vegetated areas [79]. In a rapid mapping study of river floods by Sajjad et al. [80], the MNDWI achieved an average overall accuracy of 90%, while the NDWI images had an overall average accuracy of about 85%. This was attributed to the fact that the NDWI result shows, in some areas, the mixture of water bodies with wet sand and bare soil. This was also observed in some cases, where the structured area was also confused with the water area. Nevertheless, due to its generally good performance, the MNDWI has become one of the most common water indices used in delineating open waters [67,81], as it is more advantageous in detecting wetlands in structured areas [82].

The main conclusions of this study are that these techniques are user-friendly, fast in depiction, and can be applied in various environments such as urban, agricultural, and natural landscapes. It should be noted that the NDWI can separate water from soil and vegetated surfaces. However, its limitation is that it cannot separate structured areas from water, as observed during the index mapping, while the MNDWI can effectively suppress and even remove the noise of the built environment [39]. The combination of multiple water spectral indices with thresholding can further assist in a more accurate depiction of flooded areas, depending on the environmental conditions prevailing in the area, for example, if there is intense vegetation, extensive cultivated areas, or construction in the flooded area, or if the flooded waters exhibit vegetation or other materials.

5. Conclusions

The main objective of this study was to apply a threshold method for mapping a flooded area in the northwest part of Italy along the Sesia River using Sentinel-2 multi-spectral imagery. For this purpose, the spectral indices of the NDWI and MNDWI were selected, as both are quite common and applicable for flooded-area mapping using optical

multispectral data. To assess the predicted flooded-area estimates, the relevant Copernicus emergency response product was used as a reference.

Our results showed that the NDWI somehow showed better representation, where it is also more sensitive to the separation of water from soil and vegetated areas. Sentinel-2 optical data are considered suitable for delineating a flooded area due to their high spatial resolution, especially when there are no clouds in the image. A multi-temporal approach, using multiple images from different time periods, makes the mapping of a flooded area more reliable. When radar synthetic aperture radar (SAR) image data are not available, optical multispectral data with low cloud cover are deemed sufficient for mapping flooded areas, especially when derived from the Sentinel-2 satellite, which provides a better spatial resolution compared to other freely distributed satellite data available today (e.g., Landsat).

A future goal is to map a flood event using a different validation product that can provide greater detail and better validation results. Additionally, different machine learning techniques such as Convolutional Neural Networks (CNNs) or Random Forests (RFs) can be applied, as they have been widely applied and show good results. Finally, techniques could also be explored and applied in combination with Sentinel-1 SAR images. The key advantages of the approach proposed herein include its simplicity, ease of implementation, dependence on freely distributed RS datasets, and potential for transferability to other regions. Despite the promising results of the method proposed herein, its applicability should also be confirmed in other settings and environments. In addition, further improvements in the technique proposed herein may include the examination of scenarios combining deep learning models (CNN, RF, etc.) and integrating microwave datasets into the methodological scheme. As such, the proposed methodological scheme can serve as a useful tool to support decision and policy making in moving towards a more sustainable environment concerning disaster management and, in particular, floods.

Author Contributions: Conceptualization, G.P.P., A.G. and K.K.; methodology, A.G., G.P.P. and K.K.; validation, A.G.; formal analysis, G.P.P. and K.K.; writing—original draft preparation, A.G.; writing—review and editing, A.G., G.P.P. and K.K.; visualization, A.G., G.P.P. and K.K.; supervision, G.P.P. All authors have read and agreed to the published version of the manuscript.

Funding: This research received no external funding.

Data Availability Statement: Data analysis products of this study are available upon request.

Conflicts of Interest: The authors declare no conflicts of interest.

References

1. Bolan, S.; Padhye, L.P.; Jasemizad, T.; Govarthanan, M.; Karmegam, N.; Wijesekara, H.; Amarasiri, D.; Hou, D.; Zhou, P.; Biswal, B.K.; et al. Impacts of Climate Change on the Fate of Contaminants through Extreme Weather Events. *Sci. Total Environ.* **2024**, *909*, 168388. [CrossRef]
2. Teodoro, A.C.; Duarte, L. The Role of Satellite Remote Sensing in Natural Disaster Management. In *Nanotechnology-Based Smart Remote Sensing Networks for Disaster Prevention*; Elsevier: Amsterdam, The Netherlands, 2022; pp. 189–216, ISBN 978-0-323-91166-5.
3. Teng, J.; Jakeman, A.J.; Vaze, J.; Croke, B.F.W.; Dutta, D.; Kim, S. Flood Inundation Modelling: A Review of Methods, Recent Advances and Uncertainty Analysis. *Environ. Model. Softw.* **2017**, *90*, 201–216. [CrossRef]
4. Li, Y.; Martinis, S.; Plank, S.; Ludwig, R. An Automatic Change Detection Approach for Rapid Flood Mapping in Sentinel-1 SAR Data. *Int. J. Appl. Earth Obs. Geoinf.* **2018**, *73*, 123–135. [CrossRef]
5. Zhang, X.; Chan, N.W.; Pan, B.; Ge, X.; Yang, H. Mapping Flood by the Object-Based Method Using Backscattering Coefficient and Interference Coherence of Sentinel-1 Time Series. *Sci. Total Environ.* **2021**, *794*, 148388. [CrossRef] [PubMed]
6. Kalogeropoulos, K.; Tsatsaris, A.; Stathopoulos, N.; Tsesmelis, D.E.; Psarogiannis, A.; Pissias, E. GIS & Remote Sensing for Local Development. Reservoirs Positioning. In *GeoInformatics for Geosciences Advanced Geospatial Analysis using RS, GIS & Soft Computing*; Stathopoulos, N., Tsatsaris, A., Kalogeropoulos, K., Eds.; Earth Observation; Elsevier: Amsterdam, The Netherlands, 2023; ISBN 978-0-323-98983-1.
7. Schumann, G.J.-P.; Moller, D.K. Microwave Remote Sensing of Flood Inundation. *Phys. Chem. Earth Parts A/B/C* **2015**, *83–84*, 84–95. [CrossRef]
8. Stamellou, E.; Kalogeropoulos, K.; Stathopoulos, N.; Tsesmelis, D.E.; Louka, P.; Apostolidis, V.; Tsatsaris, A. A GIS-Cellular Automata-Based Model for Coupling Urban Sprawl and Flood Susceptibility Assessment. *Hydrology* **2021**, *8*, 159. [CrossRef]

9. Refice, A.; D'Addabbo, A.; Capolongo, D. (Eds.) *Flood Monitoring through Remote Sensing*; Springer Remote Sensing/Photogrammetry; Springer International Publishing: Cham, Switzerland, 2018; ISBN 978-3-319-63958-1.
10. Kalogeropoulos, K.; Tsanakas, K.; Stathopoulos, N.; Tsesmelis, D.E.; Tsatsaris, A. Cultural Heritage in the Light of Flood Hazard: The Case of the "Ancient" Olympia, Greece. *Hydrology* **2023**, *10*, 61. [CrossRef]
11. Fountoulis, I.; Mavroulis, S. Flood Hazard Assessment in the Kladeos River Basin (Olympia—Western Peloponnese, Greece). In Proceedings of the AQUA 2008 3rd International Conference, Athens, Greece, 16–19 October 2008.
12. Wang, L.; Cui, S.; Li, Y.; Huang, H.; Manandhar, B.; Nitivattananon, V.; Fang, X.; Huang, W. A Review of the Flood Management: From Flood Control to Flood Resilience. *Heliyon* **2022**, *8*, e11763. [CrossRef] [PubMed]
13. Munawar, H.S.; Hammad, A.W.A.; Waller, S.T.; Thaheem, M.J.; Shrestha, A. An Integrated Approach for Post-Disaster Flood Management Via the Use of Cutting-Edge Technologies and UAVs: A Review. *Sustainability* **2021**, *13*, 7925. [CrossRef]
14. Munawar, H.S.; Hammad, A.W.A.; Waller, S.T. Remote Sensing Methods for Flood Prediction: A Review. *Sensors* **2022**, *22*, 960. [CrossRef]
15. Awasthi, N.; Tripathi, J.N.; Petropoulos, G.P.; Kumar, P.; Singh, A.K.; Dakhore, K.K.; Ghosh, K.; Gupta, D.K.; Srivastava, P.K.; Kalogeropoulos, K.; et al. Long-Term Spatiotemporal Investigation of Various Rainfall Intensities over Central India Using EO Datasets. *Hydrology* **2024**, *11*, 27. [CrossRef]
16. Guerriero, L.; Ruzza, G.; Guadagno, F.M.; Revellino, P. Flood Hazard Mapping Incorporating Multiple Probability Models. *J. Hydrol.* **2020**, *587*, 125020. [CrossRef]
17. JBA. Severe Storms Bring Flooding to Italy. 2018. Available online: https://www.jbarisk.com/products-services/event-response/italy-emilia-romagna-floods-may-2023/ (accessed on 2 May 2024).
18. Munawar, H.S.; Hammad, A.W.A.; Waller, S.T. A Review on Flood Management Technologies Related to Image Processing and Machine Learning. *Autom. Constr.* **2021**, *132*, 103916. [CrossRef]
19. Notti, D.; Giordan, D.; Caló, F.; Pepe, A.; Zucca, F.; Galve, J. Potential and Limitations of Open Satellite Data for Flood Mapping. *Remote Sens.* **2018**, *10*, 1673. [CrossRef]
20. Feng, Q.; Gong, J.; Liu, J.; Li, Y. Flood Mapping Based on Multiple Endmember Spectral Mixture Analysis and Random Forest Classifier—The Case of Yuyao, China. *Remote Sens.* **2015**, *7*, 12539–12562. [CrossRef]
21. Sadiq, R.; Akhtar, Z.; Imran, M.; Ofli, F. Integrating Remote Sensing and Social Sensing for Flood Mapping. *Remote Sens. Appl. Soc. Environ.* **2022**, *25*, 100697. [CrossRef]
22. Abazaj, F. SENTINEL-2 Imagery for Mapping and Monitoring Flooding in Buna River Area. *J. Int. Environ. Appl. Sci.* **2019**, *15*, 48–53.
23. Stathopoulos, N.; Kalogeropoulos, K.; Zoka, M.; Louka, P.; Tsesmelis, D.E.; Tsatsaris, A. An Integrated Approach for a Flood Impact Assessment on Land Uses/Cover Based on SAR Images & Spatial Analytics. The Case of an Extreme Event in Sperchios River Basin, Greece. In *GeoInformatics for Geosciences Advanced Geospatial Analysis Using RS, GIS & Soft Computing*; Stathopoulos, N., Tsatsaris, A., Kalogeropoulos, K., Eds.; Earth Observation; Elsevier: Amsterdam, The Netherlands, 2023; ISBN 978-0-323-98983-1.
24. Tedla, H.Z.; Bekele, T.W.; Nigussie, L.; Negash, E.D.; Walsh, C.L.; O'Donnell, G.; Haile, A.T. Threshold-Based Flood Early Warning in an Urbanizing Catchment through Multi-Source Data Integration: Satellite and Citizen Science Contribution. *J. Hydrol.* **2024**, *635*, 131076. [CrossRef]
25. Elstohy, R.; Ali, E.M. A Flash Flood Detected Area Using Classification-Based Image Processing for Sentinel-2 Satellites Data: A Case Study of Zafaraana Road at Red Sea. *Egypt. J. Remote Sens. Space Sci.* **2023**, *26*, 807–814. [CrossRef]
26. Razavi-Termeh, S.V.; Seo, M.; Sadeghi-Niaraki, A.; Choi, S.-M. Flash Flood Detection and Susceptibility Mapping in the Monsoon Period by Integration of Optical and Radar Satellite Imagery Using an Improvement of a Sequential Ensemble Algorithm. *Weather. Clim. Extrem.* **2023**, *41*, 100595. [CrossRef]
27. Teodoro, A.C.; Duarte, L. The Synergy of Remote Sensing and Geographical Information Systems in the Management of Natural Disasters. In *Nanotechnology-Based Smart Remote Sensing Networks for Disaster Prevention*; Elsevier: Amsterdam, The Netherlands, 2022; pp. 217–230, ISBN 978-0-323-91166-5.
28. Kalogeropoulos, K.; Chalkias, C. Modelling the Impacts of Climate Change on Surface Runoff in Small Mediterranean Catchments: Empirical Evidence from Greece. *Water Environ. J.* **2013**, *27*, 505–513. [CrossRef]
29. Kalogeropoulos, K.; Stathopoulos, N.; Psarogiannis, A.; Penteris, D.; Tsiakos, C.; Karagiannopoulou, A.; Krikigianni, E.; Karymbalis, E.; Chalkias, C. A GIS-Based Method for Flood Risk Assessment. In Proceedings of the EGU General Assembly Conference Abstracts, Vienna, Austria, 17–22 April 2016; Volume 18, p. 12788.
30. Du, Y.; Zhang, Y.; Ling, F.; Wang, Q.; Li, W.; Li, X. Water Bodies' Mapping from Sentinel-2 Imagery with Modified Normalized Difference Water Index at 10-m Spatial Resolution Produced by Sharpening the SWIR Band. *Remote Sens.* **2016**, *8*, 354. [CrossRef]
31. Chen, S.; Huang, W.; Chen, Y.; Feng, M. An Adaptive Thresholding Approach toward Rapid Flood Coverage Extraction from Sentinel-1 SAR Imagery. *Remote Sens.* **2021**, *13*, 4899. [CrossRef]
32. Gigović, L.; Pamučar, D.; Bajić, Z.; Drobnjak, S. Application of GIS-Interval Rough AHP Methodology for Flood Hazard Mapping in Urban Areas. *Water* **2017**, *9*, 360. [CrossRef]
33. Jiang, X.; Liang, S.; He, X.; Ziegler, A.D.; Lin, P.; Pan, M.; Wang, D.; Zou, J.; Hao, D.; Mao, G.; et al. Rapid and Large-Scale Mapping of Flood Inundation via Integrating Spaceborne Synthetic Aperture Radar Imagery with Unsupervised Deep Learning. *ISPRS J. Photogramm. Remote Sens.* **2021**, *178*, 36–50. [CrossRef]

34. Irwin, K.; Beaulne, D.; Braun, A.; Fotopoulos, G. Fusion of SAR, Optical Imagery and Airborne LiDAR for Surface Water Detection. *Remote Sens.* **2017**, *9*, 890. [CrossRef]
35. Clement, M.A.; Kilsby, C.G.; Moore, P. Multi-temporal Synthetic Aperture Radar Flood Mapping Using Change Detection. *J. Flood Risk Manag.* **2018**, *11*, 152–168. [CrossRef]
36. Xue, L.; Liu, G.; Parfitt, J.; Liu, X.; Van Herpen, E.; Stenmarck, Å.; O'Connor, C.; Östergren, K.; Cheng, S. Missing Food, Missing Data? A Critical Review of Global Food Losses and Food Waste Data. *Environ. Sci. Technol.* **2017**, *51*, 6618–6633. [CrossRef] [PubMed]
37. Konapala, G.; Kumar, S.V.; Khalique Ahmad, S. Exploring Sentinel-1 and Sentinel-2 Diversity for Flood Inundation Mapping Using Deep Learning. *ISPRS J. Photogramm. Remote Sens.* **2021**, *180*, 163–173. [CrossRef]
38. Alaghmand, S.; Abdullah, R.B.; Abustan, I.; Vosoogh, B. GIS-Based River Flood Hazard Mapping in Urban Area (a Case Study in Kayu Ara River Basin, Malaysia). *Int. J. Eng. Technol.* **2010**, *2*, 488–500.
39. Li, Y.; Dang, B.; Zhang, Y.; Du, Z. Water Body Classification from High-Resolution Optical Remote Sensing Imagery: Achievements and Perspectives. *ISPRS J. Photogramm. Remote Sens.* **2022**, *187*, 306–327. [CrossRef]
40. Goffi, A.; Stroppiana, D.; Brivio, P.A.; Bordogna, G.; Boschetti, M. Towards an Automated Approach to Map Flooded Areas from Sentinel-2 MSI Data and Soft Integration of Water Spectral Features. *Int. J. Appl. Earth Obs. Geoinf.* **2020**, *84*, 101951. [CrossRef]
41. Huang, M.; Jin, S. Rapid Flood Mapping and Evaluation with a Supervised Classifier and Change Detection in Shouguang Using Sentinel-1 SAR and Sentinel-2 Optical Data. *Remote Sens.* **2020**, *12*, 2073. [CrossRef]
42. Bangira, T.; Alfieri, S.M.; Menenti, M.; Van Niekerk, A. Comparing Thresholding with Machine Learning Classifiers for Mapping Complex Water. *Remote Sens.* **2019**, *11*, 1351. [CrossRef]
43. Lawal, U.D.; Martori, A.N.; Hashim, M.A.; Chandio, A.I.; Sabri, S.; Balogun, A.L.; Abba, A.H. Geographic Information System and Remote Sensing Applications in Flood Hazards Management: A Review. *Res. J. Appl. Sci. Eng. Technol.* **2011**, *3*, 933–947.
44. Tsatsaris, A.; Kalogeropoulos, K.; Stathopoulos, N.; Louka, P.; Tsanakas, K.; Tsesmelis, D.E.; Krassanakis, V.; Petropoulos, G.P.; Pappas, V.; Chalkias, C. Geoinformation Technologies in Support of Environmental Hazards Monitoring under Climate Change: An Extensive Review. *ISPRS Int. J. Geo-Inf.* **2021**, *10*, 94. [CrossRef]
45. Khalifeh Soltanian, F.; Abbasi, M.; Riyahi Bakhtyari, H.R. Flood Monitoring Using NDWI and MNDWI Spectral Indices: A Case Study of Aghqala Flood-2019, Golestan Province, Iran. *Int. Arch. Photogramm. Remote Sens. Spat. Inf. Sci.* 2019; XLII-4/W18, 605–607. [CrossRef]
46. Singh, K.V.; Setia, R.; Sahoo, S.; Prasad, A.; Pateriya, B. Evaluation of NDWI and MNDWI for Assessment of Waterlogging by Integrating Digital Elevation Model and Groundwater Level. *Geocarto Int.* **2015**, *30*, 650–661. [CrossRef]
47. Baig, M.H.A.; Zhang, L.; Wang, S.; Jiang, G.; Lu, S.; Tong, Q. COmparison of MNDWI and DFI for Water Mapping in Flooding Season. In Proceedings of the 2013 IEEE International Geoscience and Remote Sensing Symposium—IGARSS, Melbourne, Australia, 21–26 July 2013; pp. 2876–2879.
48. Munasinghe, D.; Cohen, S.; Huang, Y.; Tsang, Y.; Zhang, J.; Fang, Z. Intercomparison of Satellite Remote Sensing-Based Flood Inundation Mapping Techniques. *JAWRA J. Am. Water Resour. Assoc.* **2018**, *54*, 834–846. [CrossRef]
49. Albertini, C.; Gioia, A.; Iacobellis, V.; Manfreda, S. Detection of Surface Water and Floods with Multispectral Satellites. *Remote Sens.* **2022**, *14*, 6005. [CrossRef]
50. Sivanpillai, R.; Jacobs, K.M.; Mattilio, C.M.; Piskorski, E.V. Rapid Flood Inundation Mapping by Differencing Water Indices from Pre- and Post-Flood Landsat Images. *Front. Earth Sci.* **2021**, *15*, 1–11. [CrossRef]
51. Cassardo, C.; Loglisci, N.; Paesano, G.; Rabuffetti, D.; Qian, M.W. The Hydrological Balance of the October 2000 Flood in Piedmont, Italy: Quantitative Analysis and Simulation. *Phys. Geogr.* **2006**, *27*, 411–434. [CrossRef]
52. Luino, F.; Turconi, L.; Petrea, C.; Nigrelli, G. Uncorrected Land-Use Planning Highlighted by Flooding: The Alba Case Study (Piedmont, Italy). *Nat. Hazards Earth Syst. Sci.* **2012**, *12*, 2329–2346. [CrossRef]
53. Grazzini, F.; Fragkoulidis, G.; Pavan, V.; Antolini, G. The 1994 Piedmont Flood: An Archetype of Extreme Precipitation Events in Northern Italy. *Bull. Atmos. Sci. Technol.* **2020**, *1*, 283–295. [CrossRef]
54. Bozzolan, E.; Brenna, A.; Surian, N.; Carbonneau, P.; Bizzi, S. Quantifying the Impact of Spatiotemporal Resolution on the Interpretation of Fluvial Geomorphic Feature Dynamics From Sentinel 2 Imagery: An Application on a Braided River Reach in Northern Italy. *Water Resour. Res.* **2023**, *59*, e2023WR034699. [CrossRef]
55. Davolio, S.; Malguzzi, P.; Drofa, O.; Mastrangelo, D.; Buzzi, A. The Piedmont Flood of November 1994: A Testbed of Forecasting Capabilities of the CNR-ISAC Meteorological Model Suite. *Bull. Atmos. Sci. Technol.* **2020**, *1*, 263–282. [CrossRef] [PubMed]
56. Ferretti, R.; Low-Nam, S.; Rotunno, R. Numerical Simulations of the Piedmont Flood of 4–6 November 1994. *Tellus A* **2000**, *52*, 162–180. [CrossRef]
57. Cian, F.; Marconcini, M.; Ceccato, P.; Giupponi, C. Flood Depth Estimation by Means of High-Resolution SAR Images and Lidar Data. *Nat. Hazards Earth Syst. Sci.* **2018**, *18*, 3063–3084. [CrossRef]
58. Perotti, L.; Bollati, I.M.; Viani, C.; Zanoletti, E.; Caironi, V.; Pelfini, M.; Giardino, M. Fieldtrips and Virtual Tours as Geotourism Resources: Examples from the Sesia Val Grande UNESCO Global Geopark (NW Italy). *Resources* **2020**, *9*, 63. [CrossRef]
59. Nigrelli, G.; Audisio, C. The May 2008 Extreme Rain Event in the Germanasca Valley (Italian Western Alps): Processes and Effects Observed along the Hydrographic Network and Valley Slopes. *Geogr. Fis. Din. Quat.* **2009**, *32*, 157–166.
60. Nigrelli, G.; Audisio, C. Floods in Alpine River Bassins (Italy): An Interdisciplinary Study Combining Historical Information and Hydroclimatic Data. *Geogr. Fis. Din. Quat.* **2010**, *33*, 205–2013.

61. Sangati, M.; Borga, M.; Rabuffetti, D.; Bechini, R. Influence of Rainfall and Soil Properties Spatial Aggregation on Extreme Flash Flood Response Modelling: An Evaluation Based on the Sesia River Basin, North Western Italy. *Adv. Water Resour.* **2009**, *32*, 1090–1106. [CrossRef]
62. Stampoulis, D.; Anagnostou, E.N.; Nikolopoulos, E.I. Assessment of High-Resolution Satellite-Based Rainfall Estimates over the Mediterranean during Heavy Precipitation Events. *J. Hydrometeorol.* **2013**, *14*, 1500–1514. [CrossRef]
63. Scorpio, V.; Piégay, H. Is Afforestation a Driver of Change in Italian Rivers within the Anthropocene Era? *Catena* **2021**, *198*, 105031. [CrossRef]
64. Boni, G.; Ferraris, L.; Pulvirenti, L.; Squicciarino, G.; Pierdicca, N.; Candela, L.; Pisani, A.R.; Zoffoli, S.; Onori, R.; Proietti, C.; et al. A Prototype System for Flood Monitoring Based on Flood Forecast Combined With COSMO-SkyMed and Sentinel-1 Data. *IEEE J. Sel. Top. Appl. Earth Obs. Remote Sens.* **2016**, *9*, 2794–2805. [CrossRef]
65. Samuele, D.P.; Filippo, S.; Enrico, B.-M. Multi-Temporal Mapping of Flood Damage to Crops Using Sentinel-1 Imagery: A Case Study of the Sesia River (October 2020). *Remote Sens. Lett.* **2021**, *12*, 459–469. [CrossRef]
66. Volpi, M.; Petropoulos, G.P.; Kanevski, M. Flooding Extent Cartography with Landsat TM Imagery and Regularized Kernel Fisher's Discriminant Analysis. *Comput. Geosci.* **2013**, *57*, 24–31. [CrossRef]
67. Feyisa, G.L.; Meilby, H.; Fensholt, R.; Proud, S.R. Automated Water Extraction Index: A New Technique for Surface Water Mapping Using Landsat Imagery. *Remote Sens. Environ.* **2014**, *140*, 23–35. [CrossRef]
68. Billah, M.; Islam, A.K.M.S.; Mamoon, W.B.; Rahman, M.R. Random Forest Classifications for Landuse Mapping to Assess Rapid Flood Damage Using Sentinel-1 and Sentinel-2 Data. *Remote Sens. Appl. Soc. Environ.* **2023**, *30*, 100947. [CrossRef]
69. Fichtner, F.; Mandery, N.; Wieland, M.; Groth, S.; Martinis, S.; Riedlinger, T. Time-Series Analysis of Sentinel-1/2 Data for Flood Detection Using a Discrete Global Grid System and Seasonal Decomposition. *Int. J. Appl. Earth Obs. Geoinf.* **2023**, *119*, 103329. [CrossRef]
70. Nhangumbe, M.; Nascetti, A.; Georganos, S.; Ban, Y. Supervised and Unsupervised Machine Learning Approaches Using Sentinel Data for Flood Mapping and Damage Assessment in Mozambique. *Remote Sens. Appl. Soc. Environ.* **2023**, *32*, 101015. [CrossRef]
71. McFeeters, S.K. The Use of the Normalized Difference Water Index (NDWI) in the Delineation of Open Water Features. *Int. J. Remote Sens.* **1996**, *17*, 1425–1432. [CrossRef]
72. Lu, D.; Mausel, P.; Brondízio, E.; Moran, E. Change Detection Techniques. *Int. J. Remote Sens.* **2004**, *25*, 2365–2401. [CrossRef]
73. Dutta, M.; Saha, S.; Saikh, N.I.; Sarkar, D.; Mondal, P. Application of Bivariate Approaches for Flood Susceptibility Mapping: A District Level Study in Eastern India. *HydroResearch* **2023**, *6*, 108–121. [CrossRef]
74. Nasser, F.D.C.; Mello, D.C.D.; Francelino, M.R.; Krause, M.B.; Soares, H.D.M.; Demattê, J.A.M. Mapping Deactivated Mine Areas in the Amazon Forest Impacted by Seasonal Flooding: Assessing Soil-Hydrological Processes and Quality Dynamics by Remote Sensing and Geophysical Techniques. *Remote Sens. Appl. Soc. Environ.* **2024**, *34*, 101148. [CrossRef]
75. Gašparović, M.; Klobučar, D. Mapping Floods in Lowland Forest Using Sentinel-1 and Sentinel-2 Data and an Object-Based Approach. *Forests* **2021**, *12*, 553. [CrossRef]
76. Tarpanelli, A.; Mondini, A.C.; Camici, S. Effectiveness of Sentinel-1 and Sentinel-2 for Flood Detection Assessment in Europe. *Nat. Hazards Earth Syst. Sci.* **2022**, *22*, 2473–2489. [CrossRef]
77. Landuyt, L.; Verhoest, N.E.C.; Van Coillie, F.M.B. Flood Mapping in Vegetated Areas Using an Unsupervised Clustering Approach on Sentinel-1 and -2 Imagery. *Remote Sens.* **2020**, *12*, 3611. [CrossRef]
78. Liu, S.; Wu, Y.; Zhang, G.; Lin, N.; Liu, Z. Comparing Water Indices for Landsat Data for Automated Surface Water Body Extraction under Complex Ground Background: A Case Study in Jilin Province. *Remote Sens.* **2023**, *15*, 1678. [CrossRef]
79. Moradi, M.; Sahebi, M.; Shokri, M. Modified optimization water index (MOWI) for Landsat-8 OLI/TIRS. *Int. Arch. Photogramm. Remote Sens. Spat. Inf. Sci.* 2017; XLII-4/W4, 185–190. [CrossRef]
80. Sajjad, A.; Lu, J.; Chen, X.; Saleem, N. Rapid Riverine Flood Mapping with Different Water Indexes Using Flood Instances Landsat-8 Images. In Proceedings of the 5th International Electronic Conference on Water Sciences, Online, 16–30 November 2020; p. 8049.
81. Ma, S.; Zhou, Y.; Gowda, P.H.; Dong, J.; Zhang, G.; Kakani, V.G.; Wagle, P.; Chen, L.; Flynn, K.C.; Jiang, W. Application of the Water-Related Spectral Reflectance Indices: A Review. *Ecol. Indic.* **2019**, *98*, 68–79. [CrossRef]
82. Erenoğlu, R.C.; Arslan, E. Flood Analysis and Mapping Using Sentinel-1 Data: A Case Study from Tarsus Plain, Turkey. *Lapseki Mesl. Yüksekokulu Uygulamalı Araştırmalar Derg.* **2021**, *2*, 35–49.

Disclaimer/Publisher's Note: The statements, opinions and data contained in all publications are solely those of the individual author(s) and contributor(s) and not of MDPI and/or the editor(s). MDPI and/or the editor(s) disclaim responsibility for any injury to people or property resulting from any ideas, methods, instructions or products referred to in the content.